Inorganic Chemistry
Cite This: Inorg. Chem. 2019, 58, 3707−3716
Article
pubs.acs.org/IC

Interplay between Solubility Limit, Structure, and Optical Properties of Tungsten-Doped Ga_2O_3 Compounds Synthesized by a Two-Step Calcination Process

Vishal Zade,[†,§] Bandi Mallesham,[†,§] Sanjay Shantha-Kumar,[‡] Arturo Bronson,[‡] and C. V. Ramana*[,†]

[†]Centre for Advanced Materials Research (CMR), University of Texas at El Paso, 500 West University Avenue, El Paso, Texas 79968, United States

[‡]Department of Mechanical Engineering, University of Texas at El Paso, 500 West University Avenue, El Paso, Texas 79968, United States

ABSTRACT: This work unfolds the fundamental mechanisms and demonstrates the tunable optical properties derived via chemical composition tailoring in tungsten (W)-doped gallium oxide (Ga_2O_3) compounds. On the basis of the detailed investigation, the solubility limits of tungsten (W^{6+}) ion and associated effects on the crystal structure, morphology, and optical properties of W-doped Ga_2O_3 ($Ga_{2-2x}W_xO_3$, $0.00 \le x \le 0.25$, GWO) compounds are reported. GWO materials were synthesized via a conventional solid-state reaction route, where a two-step calcination is adopted to produce materials with a high structural and chemical quality. X-ray diffraction analyses of sintered GWO compounds reveal the formation of a solid solution of GWO compounds at lower concentrations W ($x \le 0.10$), while unreacted WO_3 secondary phase formation occurs at higher concentrations (x>0.10). Insolubility of W at higher concentrations ($x \ge 0.15$) is attributed to the difference in formation enthalpies of respective oxides, i.e., Ga_2O_3 and WO_3. GWO compounds exhibit an interesting trend in morphology evolution as a function of W content. While intrinsic Ga_2O_3 exhibits rod-shaped morphology, W-doped Ga_2O_3 compounds exhibit nearly spherical-shaped grain morphology. Increasing W content ($x \ge 0.10$) induces morphology transformation from spherical to faceted grains with different facets (square and hexagonal). Relatively larger grain sizes in GWO compounds might be attributed to vacancy assisted enhanced mass transport due to W incorporation and/or WO_3 induced liquid phase sintering. Our findings demonstrate a substantial red shift in band gap (E_g), which is evident from the optical absorption spectra, enabling the wide spectral selectivity of GWO compounds. W *5d* orbitals induced *sp*−*d* exchange interaction between valence band and conduction band electrons accounts for the substantial red shift in E_g of GWO compounds. Also, with increasing W, E_g decreases linearly, obeying Vegard law up to $x = 0.15$ and, at this point, an abrupt E_g drop prevails. The nonlinearity (*bowing effect*) behavior in E_g beyond $x = 0.15$ is due to insolubility of W at higher concentrations. The fundamental scientific understanding of the interdependence of synthetic conditions, structure, chemistry, and band gap could be useful to optimize GWO materials for optical, optoelectronic, and photocatalytic device applications.

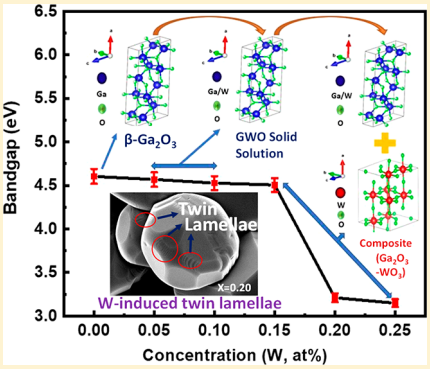

INTRODUCTION

Among the wide band gap transparent semiconducting oxides, Ga_2O_3 has gained considerable interest due to its unique properties and great potential to be applicable in modern electronic, optical, photocatalytic, and optoelectronic device technologies.[1−3] Gallium oxide is known to exhibit multiple polymorphs, viz. $\alpha, \beta, \gamma, \delta, \varepsilon$.[4,5] Among all of these polymorphs, β-phase Ga_2O_3 with its exceptional chemical and thermal stability to high temperatures is quite interesting and has been the subject of extensive recent investigations.[6−8] The crystal symmetry of β-Ga_2O_3 is monoclinic (space group: $C2/m$) with cell parameters, a = 12.214 Å, b = 3.0371 Å, c = 5.7981 Å, and β = 103.83°.[9] In the monoclinic unit cell (Figure 1), Ga occupies two different lattice positions Ga(I) with tetrahedrally coordinated oxygens and Ga(II) with octahedrally coordinated oxygens,[9,10] whereas oxygen occupies three different lattice sites [denoted as O(I), O(II), and O (III)] in distorted cubic close packed arrangement around Ga sites.[9]

β-Ga_2O_3 is the second largest wide band gap material among the available semiconductors after diamond with an optical band gap of ∼4.8 eV.[11] β-Ga_2O_3 exhibits a high dielectric breakdown voltage (8 MV) due to it high chemical and thermal stability.[6,12] Ga_2O_3 exhibits *n*-type electrical conductivity due to the presence of intrinsic oxygen defects. These unique properties make β-Ga_2O_3 materials interesting for various technological applications including, but not limited to, high power electronic devices,[13,14] solar blind UV photodetectors,[15,16] light emitting diodes,[2,17−19] photocatalyst,[20] transparent conducting oxides (TCOs),[21−23] gas sensors,[24−26] etc. However, doping of Ga_2O_3 has been widely considered

Received: November 29, 2018
Published: March 7, 2019

DOI: 10.1021/acs.inorgchem.8b03328
Inorg. Chem. 2019, 58, 3707−3716

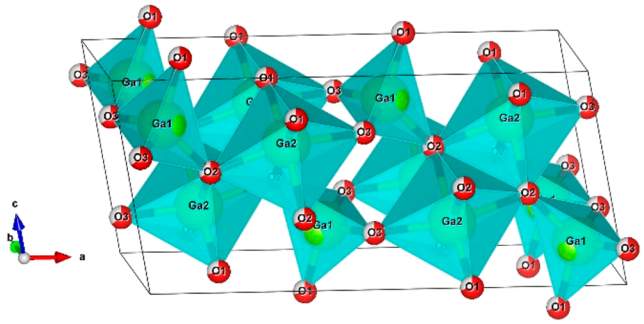

Figure 1. Monoclinic unit cell of β-Ga_2O_3.

either to realize new applications and/or to improve the performance efficiencies in these practical device applications.[13−16,20] Doping Ga_2O_3 with suitable metal ions plays a vital role in altering/enhancing its characteristic physical, chemical, optical, and electronic properties.[27,28] The effect of various donor and acceptor dopants was explored in the form of both bulk and thin films to alter their optical properties, nature of electrical conductivity (*n*-type to *p*-type), and defect chemistry for realizing a wide range of aforementioned applications.

There are quite a number of both experimental and theoretical (density functional theory calculations) reports exploring the doping effects in β-Ga_2O_3.[5,29,30] Villora et al.[31] demonstrated control over electrical conductivity of β-Ga_2O_3 by doping Si ions. Si^{4+} is an effective electron donor when it is substituted at a Ga site; hence, Si-doping increases the *n*-type conductivity due to increase in free carrier concentration about 3 orders of magnitude, as compared to undoped Ga_2O_3. Sn-doped Ga_2O_3 single crystals grown by the Float Zone method exhibit controlled carrier density and electrical resistivity with varying concentration.[16] It has been proposed that Sn-doped Ga_2O_3 ceramics could be viable candidates for GaN-based optical devices as transparent conducting oxides from the visible to deep UV region.[16] Formation energy and defect nature of *n*-type transition metal dopants, such as W, Mo, Nb, Re, were studied using density functional theory calculations.[32] The study reports that W, Mo, and Re act as deep donors, whereas Nb acts as a shallow donor with the lowest formation energy.[32] Wang et al.[33] reported that Zn^{2+}-doping remarkably enhances the photocatalytic activity of β-Ga_2O_3 due to doping-facilitated charge separation associated with heterojunction ($ZnGa_2O_4$-β-Ga_2O_3) induced band alignment, whereas doping Pb^{2+} deteriorates photocatalytic activity which is attributed to dopant generated charge recombination centers.[33] The optical band gap of as-deposited and post-annealed Cu-doped β-Ga_2O_3 polycrystalline thin films fabricated through RF magnetron sputtering decreases due to impurity energy level of Cu.[34] Also, the optical band gap of Nb-doped β-Ga_2O_3 decreases compared to intrinsic β-Ga_2O_3, the reduction in band gap of Nb-doped β-Ga_2O_3 polycrystalline in thin films associated with resultant Nb unoccupied new energy levels below the conduction band edge.[35] Similarly, a red shift in optical band gap was observed in W- and Ti-doped β-Ga_2O_3 polycrystalline thin films.[15,27,28,36] However, there are only few limited studies which demonstrate band gap engineering of Ga_2O_3 through doping so as to produce materials suitable for integration into optical devices with a spectral selectivity across the visible to UV spectral range. Specifically, there exist very few studies on W-doped Ga_2O_3 thin films with a clear red shift observed in the optical band gap. To the best of our knowledge, there are no studies available on the W-doped Ga_2O_3 bulk ceramic system, which is the focus of the present work.

Tungsten-doped Ga_2O_3 ceramics with variable W concentration were studied in detail in the present work. The GWO system is interesting to explore due to the following reasons. Shannon ionic radii of W^{6+} (tetrahedral - 0.040 nm and octahedral - 0.060 nm) and Ga^{3+} (tetrahedral - 0.047 nm and octahedral - 0.062 nm)[37] in both tetrahedral and octahedral coordinations are closely in match with each other, in addition to comparable electronegativity (Ga-1.82,[38] W-2.36[39]) values, and it suggests that the electronic properties can be tuned while retaining the parent crystal structure unperturbed. However, despite comparable ionic radii and electronegativity, studies available in the literature on the W-incorporated Ga_2O_3 thin films reported on that amorphization occurs even for relatively lower W content and complete solid solution is possible only for a limited W concentration.[16,29] It must be noted that the ability to tune the processing conditions, particularly the deposition temperature required to produce crystalline materials in either chemical (CVD) or physical vapor deposition (PVD) methods of thin film fabrication, is limited. Furthermore, the CVD and PVD methods rely on nonequilibrium processes, where energetic ions will be taking part in thin film material production.[40−42] Therefore, the true solubility limits of the compound material system and required processing temperatures required may not reflect the efficient means to understand the fundamental limits of solid solution formation. On the other hand, the high-temperature solid-state chemical reaction method is a simple, versatile method to produce chemical compounds, where the solubility limits and component mixtures can be easily understood and/or manipulated. Hence, W-doped Ga_2O_3 ceramics provide a deeper, fundamental understanding into these materials in terms of solubility limit of W and provide efficient means to tailor the structure and electronic properties. Therefore, in the present work, the effect of W-doping on the structural, morphological, and optical properties of Ga_2O_3 ceramics ($Ga_{2-2x}W_xO_3$, $0 \leq x \leq 0.25$) and their correlation to solubility limit of W ions has been studied in detail.

EXPERIMENTAL METHODS

Synthesis. $Ga_{2-2x}W_xO_3$ (GWO) compounds were synthesized by conventional solid-state reaction method by varying the composition in the range $0 \leq x \leq 0.25$. High purity metal oxide powder precursors Ga_2O_3 (99.99%) and WO_3 (99.9% purity) were procured from Sigma-Aldrich. To synthesize GWO compounds, procured high purity precursors were weighed in stoichiometric proportion with respect to desired composition. The weighed powders were collected in an agate mortar and pulverized using acetone as wetting medium to obtain homogeneously mixed GWO compounds. The homogeneously mixed powders were calcined at different temperatures (1050 °C, 12 h and 1150 °C, 12 h) in a muffle furnace by intermediate grinding to reach the complete solid-state reaction. Calcined powders are again ground to reduce the particle size to enhance the sinterability. Polyvinyl alcohol (PVA) was added to pulverized powders after calcination, and they were pelletized into circular discs (8 mm diameter; 1 mm thickness) using a uniaxial hydraulic press by applying a load of 1.5 ton. The obtained green pellets were sintered at 1250 °C for 6 h with a ramp rate of 5 °C, and binder burnout of pellets was ensured by holding at an intermediate temperature (500 °C) for 30 min. The crystal structure, morphology, and optical properties of sintered pellets were further characterized using X-ray diffraction coupled with

DOI: 10.1021/acs.inorgchem.8b03328
Inorg. Chem. 2019, 58, 3707−3716

Reitveld refinement, scanning electron microscopy, and UV−vis spectrophotometry.

Characterization. *X-ray Diffraction (XRD).* The phase composition and crystal structure of synthesized GWO ceramics (calcined and sintered) were verified by XRD analysis, and the patterns were collected using a Rigaku Benchtop powder X-ray diffractometer (Mini Flex II). Scanning parameters were: 10−80° (2θ range), step size - 0.02° and scan rate - 0.6°/min. Reitveld structural refinement of experimental diffraction patterns was carried out using Fullprof Software.

Scanning Electron Microscopy (SEM). Microstructural features of sintered pellets were analyzed using Scanning Electron microscopy (Hitachi - 4800). Prior to imaging, the samples were sputter coated with silver to avoid the charging effect, a common problem in imaging insulating samples.

UV−Visible−NIR Spectroscopy. The energy band gap between valence and conduction bands can be determined from the optical absorption edge associated with charge transfer from the valence band to conduction band. The optical absorption spectra are highly sensitive to crystal symmetry, nature of hybridization between atomic orbitals in a given compound, impurities, and defects. Understanding the optical absorption spectra gives more insight into elemental doping in the parent phase than X-ray diffraction analysis. The optical absorption spectra of GWO sintered powders were collected using a UV−vis spectrophotometer (PerkinElmer, Model: Lambda 1050).

RESULTS AND DISCUSSION

Crystal Structure and Refinement. The XRD patterns of GWO powders calcined at 1050 and 1150 °C for 12 h are shown in Figure 2 (a) and (b), respectively. The XRD patterns of GWO calcined at 1050 °C clearly reveal insolubility of WO_3 even at lower concentrations. The XRD peaks corresponding to unreacted WO_3 precursor are as indicated in Figure 2a. The insolubility of WO_3 in Ga_2O_3 at 1050 °C is attributed to two factors. The first is that, commonly, solid-state reaction is associated with a high temperature diffusion limited process, and the GWO system may require temperatures higher than 1050 °C to stimulate the diffusion process and form a stable solid solution. Another factor may be the difference in chemical potentials which accounts for the limited solubility of WO_3 in Ga_2O_3, though the ionic radii of W^{6+} and Ga^{3+} are comparable. However, to further confirm the solubility limit of W^{6+} at Ga lattice sites of monoclinic Ga_2O_3, another calcination of powders was done at 1150 °C. The XRD data of powders calcined (Figure 2b) at 1150 °C show diffraction peaks corresponding to WO_3 at x = 0.25. The observed solubility of W in Ga_2O_3 is consistent with that recently reported W-doped Ga_2O_3 thin films.[36] However, to the best of our knowledge, there are no studies aimed at the determination of tungsten solubility in Ga_2O_3-WO_3 ceramics. Exploring the solubility limit in GWO ceramics gives insight into functional properties of the GWO system. Hence, after two-step calcination at relatively higher temperatures (1050 and 1150 °C), the samples were sintered at 1250 °C for 6 h.

Figure 3 shows the XRD patterns of GWO compounds sintered at 1250 °C. The diffraction peaks indexed in reference

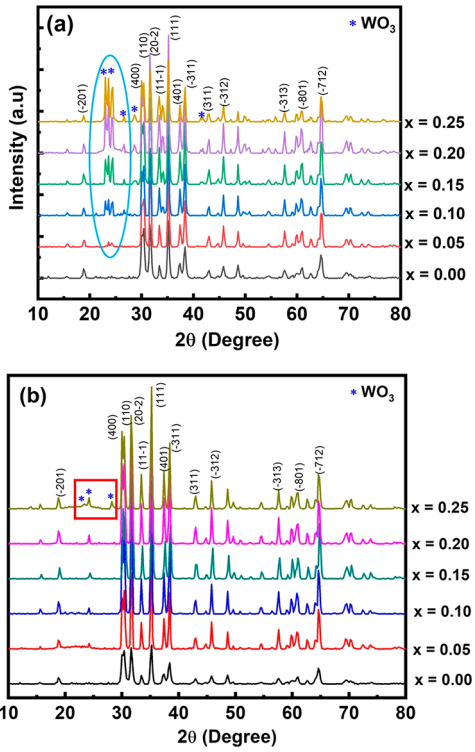

Figure 2. X-ray diffraction of patterns of $Ga_{2-2x}W_xO_3$ ($0 \le x \le 0.25$) compounds calcined at (a) 1050 °C for 12 h, (b) 1150 °C for 12 h.

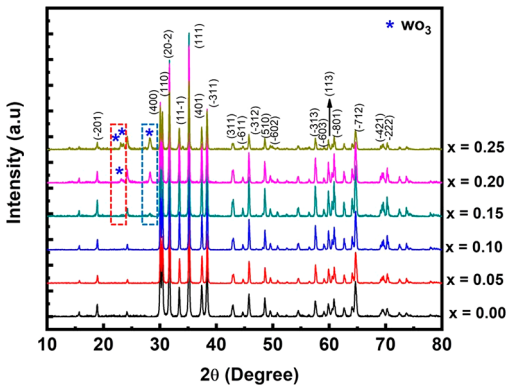

Figure 3. X-ray diffraction of patterns of $Ga_{2-2x}W_xO_3$ ($0 \le x \le 0.25$) compounds sintered at 1250 °C for 6 h.

to the crystallographic information file obtained from Rietveld refinement of diffraction patterns will be discussed in the following sections. Interestingly, after sintering, in contrast to calcined compounds, a trace amount of unreacted WO_3 phase is found only for $x \ge 0.15$. The diffraction peaks appeared due to WO_3 are indicated by asterisks. Figure 4 shows enlarged profiles of (400), (110), and (111) peaks. Due to smaller ionic radius of W^{6+}, as compared to Ga^{3+}, the XRD peaks are shifting toward higher angle until tungsten concentration of x = 0.1. This is due to the shrinkage in unit cell volume upon W ion incorporation into Ga-oxide. The peak shift magnitude is not uniform for different Bragg planes that clearly indicates the formation of GWO solid solution for $x \le 0.1$. Whereas, at $x \ge 0.15$, such behavior of peak shift could not be observed that might be due to compensating compressive strains owing to the presence of unreacted WO_3 phase. In order to derive a comprehensive understanding and quantification of solubility limits, volume fraction of unreacted WO_3 phase is calculated using[43,44]

$$\text{Volume fraction of unreacted } WO_3 = \frac{I_{(112)}WO_3}{I_{(111)}Ga_2O_3 + I_{(112)}WO_3} \times 100 \quad (1)$$

DOI: 10.1021/acs.inorgchem.8b03328
Inorg. Chem. 2019, 58, 3707−3716

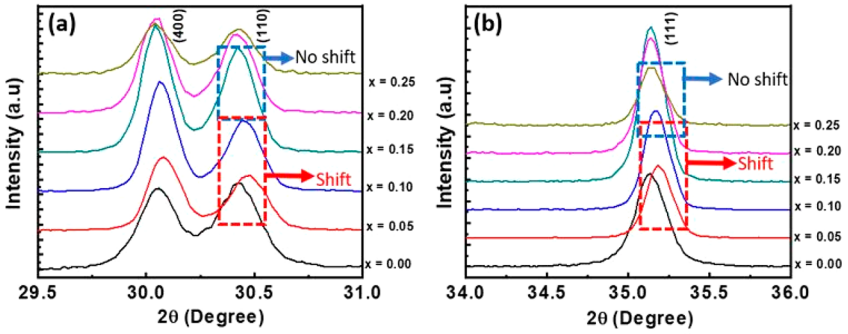

Figure 4. Enlarged diffraction profiles of (400), (110), and (111) peaks.

The amounts of unreacted WO_3 in GWO compositions with $x \geq 0.15$ are 2.5%, 8.4%, and 9.3%, respectively. The unreacted phase is approximately corroborated with calculated stochiometric proportions of the reacted and unreacted GWO system. Hence, there is a solubility limit of WO_3 in Ga_2O_3 to form a clear GWO solid solution without any traces of unreacted WO_3. Though ionic radii of W^{6+} and Ga^{3+} are comparable, the formation energy of W^{6+} in the Ga_2O_3 lattice determines the solubility limit of W. The formation energy and/or enthalpy of formation of solid solution is discussed as follows.

The concentration of doping in a given compound is determined by the formation energy of a specific defect or impurity at the parent lattice site.[30,32] In accordance with recent reports on metal doping in Ga_2O_3 using hybrid density functional theory (DFT), the formation energy of W on a Ga site is given by[32]

$$E^{f}(W_{Ga}^{q}) = E_{tot}(W_{Ga}^{q}) - E_{tot}(Ga_2O_3) - (\mu_W + \mu_W^{o}) + (\mu_{Ga} + \mu_{Ga}^{O}) + q(E_F + E_{VBM}) + \Delta^{q} \quad (2)$$

where $E_{tot}(W_{Ga}^{q})$ - total energy of one W_{Ga} in charge state q, $E_{tot}(Ga_2O_3)$ - the formation energy of undoped Ga_2O_3, E_F - Fermi energy, E_{VBM} - valence band maximum. Moreover, μ_W and μ_{Ga} are the chemical potentials with reference to total energy of the metal bulk and μ_O is chemical potential of O atom with reference to an O_2 molecule.[32]

Ga_2O_3 is formed when Ga and O chemical potentials fulfill the thermodynamic stability of Ga_2O_3 bulk compound as follows

$$2\mu_{Ga} + 3\mu_O = \Delta H_f\ (Ga_2O_3) \quad (3)$$

where $\Delta H_f\ (Ga_2O_3)$ - enthalpy of formation of bulk Ga_2O_3; the reported formation enthalpy of Ga_2O_3 is −10.73 eV.[32] Substitutional doping of W at a Ga site in bulk Ga_2O_3 and its solubility in the lattice is determined by W chemical potential and formation enthalpy of $\Delta H_f\ (WO_3)$, which is given by

$$2\mu_W + 3\mu_O = \Delta H_f\ (WO_3) \quad (4)$$

The calculated formation enthalpy of WO_3 is −7.93 eV.[32] Hence, due to the relatively higher difference in formation enthalpies of WO_3 and Ga_2O_3, W solubility at the Ga site in Ga_2O_3 is limited to 10 at %. The crystallite size of the GWO compounds was determined using Scherrer's relation

$$D = \frac{0.9\lambda}{\beta \cos\theta} \quad (5)$$

where D - crystallite size, λ (CuKα) - 1.5406 Å, β - full width at half-maximum, θ - diffraction angle. The estimated crystallite size was found to be increasing with W incorporation. However, at the very initial concentration (x = 0.05), there is a considerable increment in the crystallite size, which increased from ∼40 nm (intrinsic Ga_2O_3) to ∼50 nm (5 at % W-doped Ga_2O_3). No appreciable variation in crystallite size is noted with a further increase in W concentration.

Figure 5 shows the refined XRD patterns, where the experimental, simulated, and difference curves are shown. The

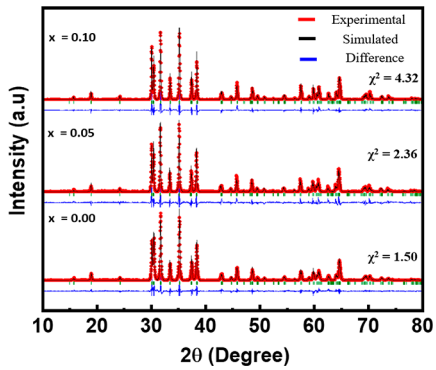

Figure 5. Refined X-ray diffraction of patterns of $Ga_{2-2x}W_xO_3$ ($0 \leq x \leq 0.1$) compounds sintered at 1250 °C for 6 h.

monoclinic crystal symmetry model with $C2/m$ space group was used to refine the experimental patterns. Experimental XRD patterns were simulated with the Pseudo Voigt peak shape function using Fullprof Software.[45] The simulated and experimental patterns were fitted with a low-intensity difference curve. The goodness of fit (χ^2) values determine the quality of refinement, and the obtained χ^2 values for refined compounds include: 1.50 (x = 0), 2.36 (x = 0.05), and 4.32 (x = 0.10). The goodness of fit values and smaller difference intensities of simulated and experimental patterns reveal that W-doped compounds were stabilized in monoclinic symmetry, i.e., similar to intrinsic Ga_2O_3. The refined structural parameters are summarized in Table 1.

Morphology and Microstructure. Figure 6 shows the SEM images of GWO compounds sintered at 1250 °C for 6 h. Parent Ga_2O_3 exhibits a rod-shaped grain morphology, with rod sizes varying approximately from 0.5−2.0 μm (width) and 1.0−4.0 μm (length). Interestingly, W incorporation into Ga_2O_3 drastically changed the grain morphology even at smaller concentrations. At lower concentrations of W (x = 0.05), grains are nearly spherical. With increasing W concentration ($x \geq 0.1$), a change in morphology was noticed from spherical to faceted grains with different facets (square and hexagonal). The faceted morphology is more visible and

DOI: 10.1021/acs.inorgchem.8b03328
Inorg. Chem. 2019, 58, 3707−3716

Table 1. Structural Parameters of GWO Compounds

W concentration	atoms	atomic coordinates			
		X	*y*	*Z*	U_{iso}
0.00	Ga1	0.08954	0.00000	0.79383	0.00832
	Ga2	0.15852	0.50000	0.31006	0.01348
	O1	0.15196	0.00000	0.10012	−0.045(5)
	O2	0.17226	0.00000	0.56402	−0.039(5)
	O3	−0.00800	0.50000	0.26455	−0.058(5)
0.10	Ga1	0.09206	0.00000	0.79531	0.00191
	Ga2	0.15634	0.50000	0.30981	0.01188
	O1	0.16045	0.00000	0.09886	0.00916
	O2	0.16528	0.00000	0.56417	−0.0056
	O3	−0.0045	0.50000	0.24983	−0.0325
	W1	0.09206	0.00000	0.79531	0.00191
	W2	0.15634	0.50000	0.30981	0.01188

significant in GWO compositions with $x \geq 0.15$.[46−48] Also, the grain size increases with increasing W concentration from x = 0.05 to x = 0.1, and beyond x = 0.1, the grain growth is almost hindered without considerable change. The grain growth in W-incorporated Ga_2O_3 compounds may be due to vacancy assisted enhanced mass transport or WO_3 induced liquid phase sintering. Liquid phase sintering might be possible in the Ga_2O_3-WO_3 system due to the low melting point of WO_3 [1473 °C][49] compared to Ga_2O_3 [1795 °C].[50] It has been reported in the literature that WO_3 addition as a sintering aid to refractory ceramics reduces the sintering temperature significantly and enhances the sinterability of the samples.[51,52] WO_3 will lead to the formation of a eutectic composition with respective material with a lower melting, and hence, liquid phase assisted sintering behavior was found in some WO_3 added compounds.[51,52] However, in the present case, we propose the liquid phase sintering as one of the possible reasons for grain growth if the Ga_2O_3-WO_3 system will form a eutectic composition with low melting. The hindering of grain growth beyond x > 0.1 of W concentration is associated with grain boundary pinning due to segregation of unreacted WO_3 at grain boundaries. The red circles in Figure 6 (x = 0.20 and x = 0.25) indicate the unreacted WO_3 phase. The unreacted WO_3 is evident at higher concentrations from X-ray diffraction analysis. In addition, grain growth was not uniform and an abnormal growth in a few grains was observed. Abnormal grain growth of some grains in W-doped Ga-oxide compounds is attributed to the growth of large particles at the expense of small particles in order to minimize the overall free energy. Such abnormal grain growth in solid-state sintering is mainly driven by the difference in mass transport of different species, which arises from the difference in chemical potentials of constituent elements. Interestingly, W-doped Ga-oxide compounds exhibit twin lamellas within a grain; such twin lamellae are more predominant at higher concentrations. In Figure 7,

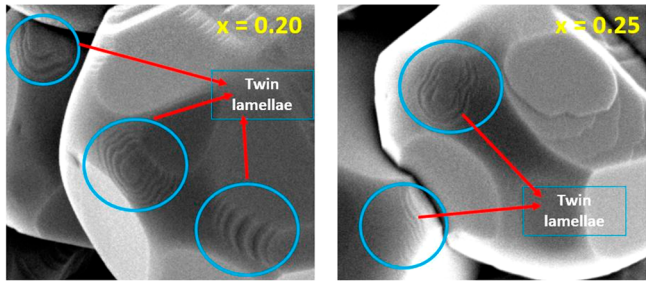

Figure 7. Enlarged SEM images of selected GWO compositions (x = 0.20, 0.25).

the enlarged images of high concentration compounds are shown to reveal the W induced twin lamellae. The formation of twin lamellas is attributed to abnormal grain growth driven by WO_3 induced enhanced vacancy diffusion or liquid phase sintering. The similar abnormal grain growth induced twin lamellas were found in donor-doped $BaTiO_3$ ceramics.[53]

Phase Equilibria of the Ga-W-O System. An attempt is made to establish the phase equilibria in the Ga-W-O ternary system from the calculations. Although the doping of W into Ga_2O_3 was ≤ 0.1 mole fraction, the phase equilibria for the Ga-W-O system was briefly examined for understanding the mechanisms involved in GWO compound formation. Wreidt[54] assessed the W-O phase diagram with WO_2 melting incongruently at 1530 °C to a two-phase field of W-$W_{18}O_{49}$ and WO_3 melting congruently at 1474 °C as W melts at 3422 °C. Between the WO_2 and WO_3, the liquidus and eutectic temperatures occur between 1430 and 1600 °C for a number of W oxides (e.g., $W_{18}O_{49}$ and W_nO_{3n-2}). A calculated Ga-W-O ternary phase diagram indicates a two-phase field of W and Ga_2O_3 with FactSage,[55] as shown in Figure 8. Three W oxides are shown on the Ga-W-O phase diagram, although the series

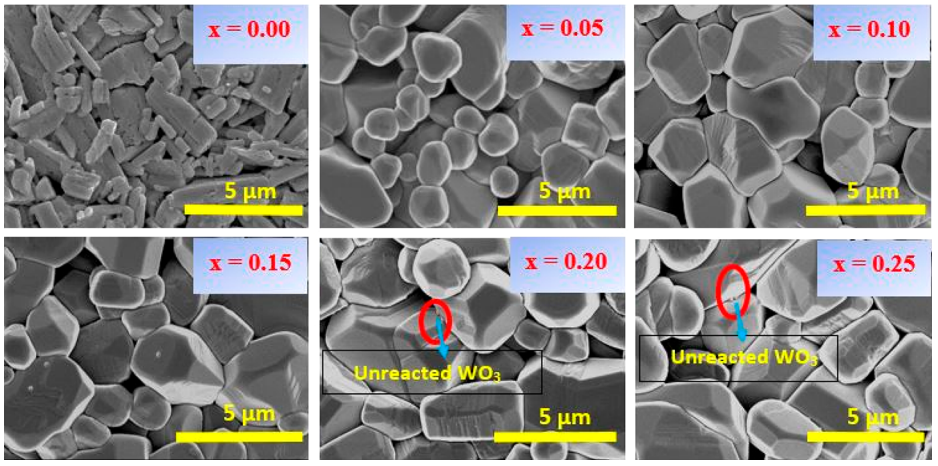

Figure 6. Microstructural features of $Ga_{2-2x}W_xO_3$ ($0 \leq x \leq 0.25$) compounds sintered at 1250 °C for 6 h.

DOI: 10.1021/acs.inorgchem.8b03328
Inorg. Chem. 2019, 58, 3707−3716

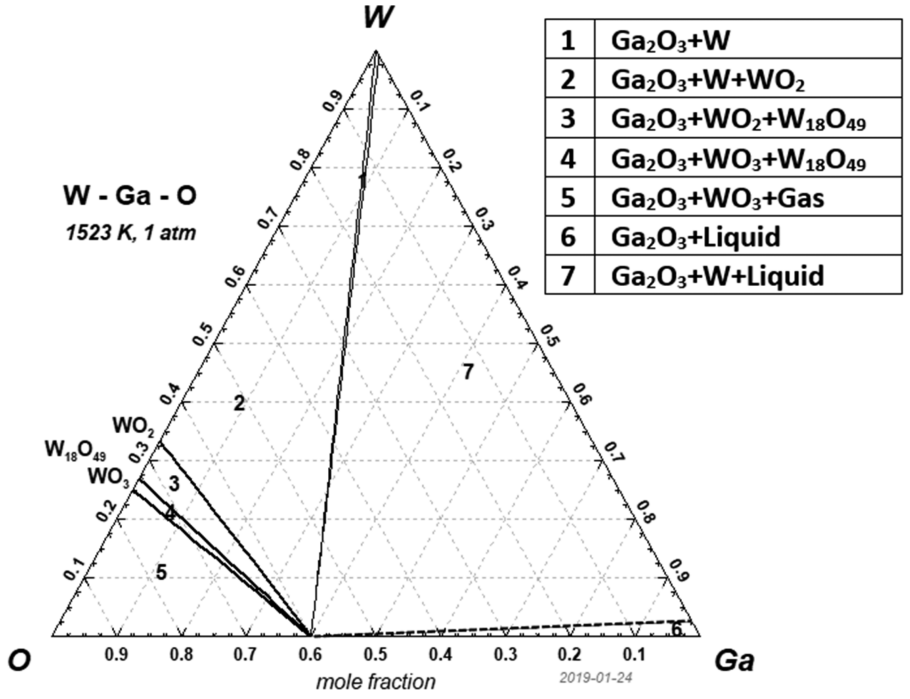

Figure 8. Ternary phase equilibria of W-Ga-O@1523K (Factsage7.2).

of W_nO_{3n-2} phases are avoided to focus on WO_3. Liquid Ga occurs in a small region on the lower right side of the Ga-W-O system and bounded by a three-phase field of Ga_2O_3-W-liquid. The two-phase field of Ga_2O_3-WO_3 indicated by the line connecting the oxides of Ga_2O_3 and WO_3 on the calculated ternary phase diagram does not show a liquid region. However, if the WO_3 forms, it is possible to form a liquid phase with the oxidation of tungsten within a grain boundary upon the diffusion of oxygen.

Optical Properties. Figure 9 shows the optical absorption spectra of $Ga_{2-2x}W_xO_3$ compounds. Intrinsic Ga_2O_3 shows

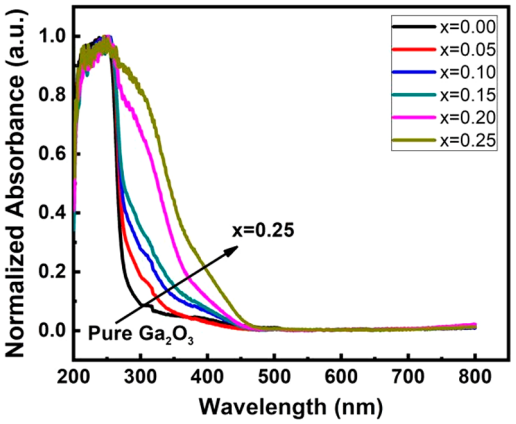

Figure 9. Optical absorption spectra of $Ga_{2-2x}W_xO_3$ ($0 \le x \le 0.25$) compounds sintered at 1250 °C for 6 h.

optical transparency in the visible and near-UV regions and exhibits an absorption edge at ≈280 nm in the UV region in accordance with the literature.[56] A clear trend and red shift of the absorption edge is noted in W-doped Ga_2O_3 compounds. A red shift observed in the optical absorption edge is prominent in GWO compounds with higher W content ($x \ge 0.20$). While red shift is also reported for W-doped Ga_2O_3 polycrystalline thin films,[36,57] the observed shift in these GWO ceramics is substantially higher compared to that reported for GWO thin films. We believe that understanding the optical properties of W-doped Ga_2O_3 ceramics, therefore, gives more insights into fundamental scientific aspects and enhances our ability to engineer the GWO compounds with desired properties and performance. Optical absorption is an atomistic phenomenon where hybridization of atomic orbitals of different elements and specific phases of the compound (crystal structure) play a crucial role in determining the optical band gap of a chemical compound. In GWO compounds, the solubility of W in the Ga_2O_3 lattice is limited, as evident from XRD analyses and structure refinement. Hence, we believe that there is a clear distinction and behavioral contrast in optical absorption features of phase pure GWO compounds versus GWO compounds with secondary phase formation. Therefore, to further understand the optical properties, the band gap of GWO compounds was calculated from the absorption spectra using a well-known Tauc method.[58,59] The Tauc relation is given by

$$\alpha h\nu = A(h\nu - E_g)^n \tag{6}$$

where α - an absorption coefficient, $h\nu$ - incident photon energy, A - proportionality constant, E_g - band gap, n - index determining the electronic transitions type (n takes values of 1/2 for direct allowed transition, 2 for indirect allowed transition, 3/2 for direct forbidden transition, and 3 for indirect forbidden transition). In UV−vis reflectance/absorption spectra, absorbance is equivalent to the Kubelka−Munk function $[F(R)]$.[60−62] The absorption coefficient is directly proportional to the Kubelka−Munk function, and the relation is expressed as[63]

$$F(R) = \frac{(1-R)^2}{2R} = \frac{K}{S} \tag{7}$$

DOI: 10.1021/acs.inorgchem.8b03328
Inorg. Chem. 2019, 58, 3707−3716

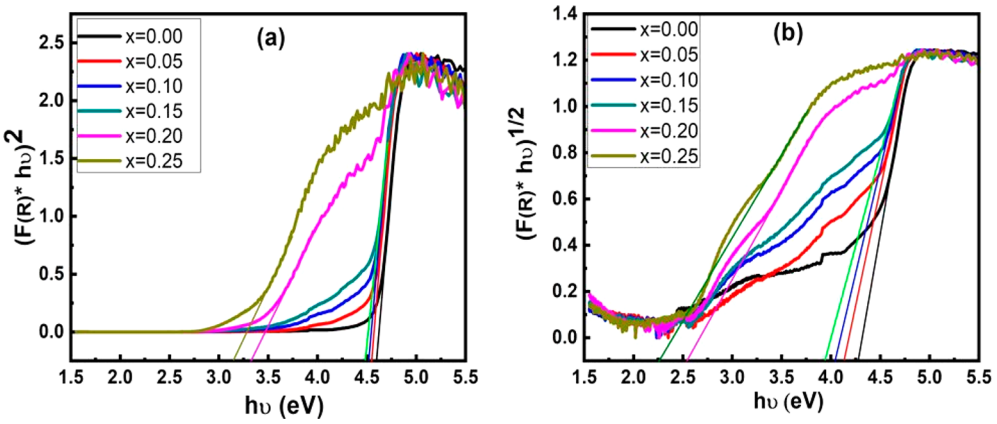

Figure 10. Tauc plots of $Ga_{2-2x}W_xO_3$ ($0 \leq x \leq 0.25$) compounds. (a) Direct band gap, (b) indirect band gap.

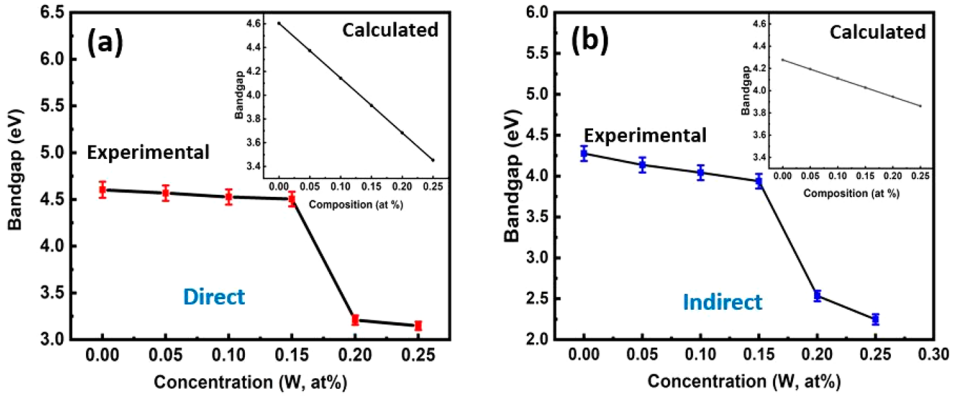

Figure 11. Optical absorption spectra of $Ga_{2-2x}W_xO_3$ ($0 \leq x \leq 0.25$) compounds sintered at 1250 °C for 6 h. (a) Direct band gap, (b) indirect band gap.

where R - reflectance, K - absorption coefficient, and S - scattering factor.

The Tauc method was used to calculate the band gap values by considering the experimentally obtained absorbance equivalent to the Kubelka–Munk function. Figure 10 shows the Tauc plots (a) $[F(R)*h\nu]^2$ vs $h\nu$ and (b) $[F(R)*h\nu]^{1/2}$ vs $h\nu$, used to determine the direct and indirect band gaps of GWO compounds, respectively. The extrapolation of the linear portion of these curves to zero absorption (x-axis) provides the band gap value. Tauc plots for both direct and indirect transitions exhibit a linear relationship, which clearly indicates that GWO compounds exhibit both direct and indirect band transitions. Theoretical and experimental findings show that β-Ga_2O_3 is known to exhibit both direct and indirect band gaps with the indirect band gap value being lower than direct band gap values.[56] The reported direct and indirect band gaps calculated using hybrid density functional theory are 4.88 and 4.84 eV,[11] while experimentally determined direct and indirect band gaps in β-Ga_2O_3 single crystals are 4.48 and 4.43 eV.[64] Both theoretically and experimentally, a small energy difference was noticed between direct and indirect band transitions (theoretical - 0.04 eV, experimental - 0.05 eV). In the present study, the determined direct and indirect band gap values are 4.60 and 4.27 eV, respectively. Interestingly, we have observed relatively higher energy difference (0.33 eV) between direct and indirect transitions in β-Ga_2O_3 ceramics. The observed direct band gap was in accordance with the literature, whereas a lower indirect band gap was found to be comparable with literature studies.[11,64] The lower indirect gap in β-Ga_2O_3 bulk ceramics than the reported values might be associated with (a) high temperature processing (solid-state reaction method) induced lattice strain[65] and (b) relatively higher point defects in bulk ceramics than that in single crystals. However, such energy difference is higher in W-doped compounds and the difference increases with increasing W concentration. A significant energy difference (0.9 eV) between direct and indirect transitions is noted for GWO compounds with the highest W concentration (x = 0.25).

In Figure 11, the variation of direct (a) and indirect band gap (b) of GWO compounds is shown as a function of W content. Both direct and indirect band gaps decrease with increasing W concentration. At lower W concentrations ($x \leq$ 0.15), the band gap decreases gradually; however, an abrupt change associated with a significant drop in band gap occurs for x = 0.2. The band gap reduction noted in GWO compounds is due to $sp-d$ exchange interaction arising from the localized electrons of W 5d orbitals. In pure Ga_2O_3, the O p orbitals contribution to valence and conduction bands is predominantly due to Ga 4s character, whereas, in W-doped compounds, the conduction band is dominated by W 5d along with Ga 4s character. Hence, the contribution of W 5d orbitals to the conduction band leads to $sp-d$ exchange interaction between valence band delocalized electrons (O s and p orbitals) and conduction band localized electrons (W 5d orbitals) in GWO compounds. The $sp-d$ exchange interaction makes positive and negative corrections to the valence band and conduction band, respectively, that results in band narrowing of GWO compounds.[66−68]

DOI: 10.1021/acs.inorgchem.8b03328
Inorg. Chem. 2019, 58, 3707−3716

The abrupt change with a substantial drop in band gap noted in GWO at $x = 0.2$ can be explained as follows. In a complete solid solution of two parent compounds (Ga_2O_3 and WO_3 in the present study), E_g and concentration x follow the Vegard law (linear relation) similar to semiconductor alloys.[69] In the present case, the Vegard law is expressed as

$$E_g(\mathrm{GWO}) = (1 - x)[E_g(Ga_2O_3)] + x[E_g(WO_3)] \quad (8)$$

where $E_g(Ga_2O_3)$ is the band gap of intrinsic Ga_2O_3 while $E_g(WO_3)$ is that of intrinsic WO_3.

The calculated band gap (direct and indirect) variation from the parent compounds [Ga_2O_3; 4.60 eV (direct), 4.27 (indirect) taken from this work) and for WO_3, 3.52 eV (direct) and 2.62 (indirect)][29,70] in accordance with the Vegard expression is shown in the inset of Figures 11a and 12b.

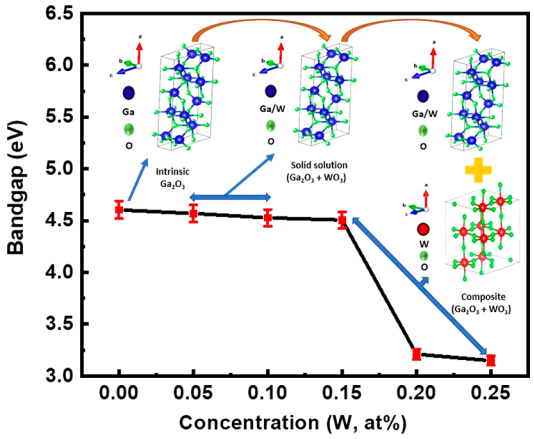

Figure 12. Representing correlation between structural modifications and band gap (direct) with varying W concentration.

It can be clearly observed from these plots that both direct and indirect band gap values show a linear variation with concentration x (W at %). However, in the present study, a *nonlinear band gap variation* with W concentration and sudden drop ($x = 0.2$) is attributed to insolubility of W in Ga_2O_3 lattice at higher concentrations.

Finally, to correlate the structural modifications and band gap (direct) with varying W concentration, the schematic representation of band gap variation coupled with structure evolution is presented in Figure 12. As discussed, intrinsic Ga_2O_3 is monoclinic, and, with W doping at $x \leq 0.1$, a clear solid solution is formed, whereas the $Ga_2O_3 + WO_3$ composite appeared at higher concentrations ($x \geq 0.15$). The band gap changes corroborate with the corresponding structural and chemical composition variations as a function of W content in GWO compounds. However, an abrupt and significant drop in band gap found at $x = 0.20$ is in direct correlation with the formation of a $Ga_2O_3 + WO_3$ composite instead of a single-phase compound. This abrupt change specifically at $x = 0.20$, as opposed to $x = 0.15$ or lower concentration of W, can easily be understood from XRD analysis. The unreacted or secondary WO_3 phase is only a fraction (2.5%), and hence, it shows minimal influence on band gap. The minimal influence on band gap at low concentration (2.5%) of unreacted phase might be attributed to a discontinuous WO_3 phase on the surface. The electronic structure changes, thus, become dominant once the secondary phase (WO_3) content in the Ga_2O_3-WO_3 composite increases to a reasonable amount.

SUMMARY AND CONCLUSIONS

A systematic and detailed investigation performed on the W-doped Ga_2O_3 ($Ga_{2-2x}W_xO_3$, $0.00 \leq x \leq 0.25$) ceramic materials provided fundamental insights into the solubility limits and effect of W-doping on the crystal structure, morphology, and optical properties of Ga_2O_3. The GWO materials were synthesized via a conventional solid-state reaction route, where involving a two-step calcination process can produce materials with a high structural and chemical quality. W ions enter into the intrinsic β-Ga_2O_3 lattice without any perturbation. That is, a solid solution of GWO compounds is readily possible up to a W concentration of $x \leq 0.10$, and above this point, the unreacted WO_3 secondary phase formation occurs. The insolubility of W at higher concentrations ($x \geq 0.15$) with a secondary WO_3 phase is primarily derived from the difference in formation enthalpies of respective oxides, i.e., Ga_2O_3 and WO_3. Interestingly, W-doping predominantly alters the Ga_2O_3 microstructure from rod-shaped morphology to nearly spherical grains consisting of square and hexagonal facets. This aspect assures that there may be further options to modify the chemical synthetic procedures and obtain morphologies that can enhance the properties and performance of doped Ga_2O_3 compounds at the nanoscale dimensions. The GWO compounds exhibit relatively large grain sizes due to WO_3 assisted vacancy enhanced mass transport or liquid phase sintering. Abnormal grain growth induced twin lamellae found in GWO compounds, which are particularly predominant at higher concentrations. The W-doping induced changes in the electronic structure and band gap are evident in the optical absorption spectra. All the GWO compounds exhibit a red shift with W-doping. The structural transformation sequence, i.e., from monoclinic Ga_2O_3 to GWO solid solution and then to finally Ga_2O_3-WO_3 composite with increasing W content, induces changes in band gap. Further, the crystal structure analysis provides fundamental insights into such red shift GWO compounds; the $sp-d$ exchange interaction between valence band and conduction band electrons originating from W $5d$ orbital electrons accounts for such red shift. In addition, the band gap shows linear behavior (Vegard law) with increasing W concentration up to $x \leq 0.15$ at %, whereas, at $x = 0.2$ at %, band gap decreases considerably and deviates from Vegard law. The nonlinearity *(bowing effect)* in band gap might be due to insolubility of W at higher concentrations. Similar to Ga_2O_3, both direct and indirect band transition behavior was found in GWO compounds. In contrast to Ga_2O_3, a relatively higher energy difference between direct and indirect band transitions was found in W-doped compounds. The fundamental scientific understanding of the interdependence of synthetic conditions, crystal structure, chemistry, and optical properties observed in GWO compounds may be applicable to a large class of refractory metal-doped Ga_2O_3 and could be useful to optimize such Ga_2O_3-based materials for optical, optoelectronic, and photocatalytic device applications.

AUTHOR INFORMATION

Corresponding Author

*E-mail: rvchintalapalle@utep.edu.

ORCID

C. V. Ramana: 0000-0002-5286-3065

Author Contributions

§Equally contributed to the work.

DOI: 10.1021/acs.inorgchem.8b03328
Inorg. Chem. 2019, 58, 3707−3716

Notes

The authors declare no competing financial interest.

■ ACKNOWLEDGMENTS

The authors acknowledge, with pleasure, support from the National Science Foundation (NSF) with NSF-PREM grant no. DMR-1827745. This material is also based upon work supported by the Air Force Office of Scientific Research under award number FA9550-18-1-0387. However, any opinions, finding, and conclusions or recommendations expressed in this material are those of the author(s) and do not necessarily reflect the views of the United States Air Force.

■ REFERENCES

(1) Higashiwaki, M.; Sasaki, K.; Kuramata, A.; Masui, T.; Yamakoshi, S. Gallium oxide (Ga_2O_3) metal-semiconductor field-effect transistors on single-crystal β-Ga_2O_3 (010) substrates. *Appl. Phys. Lett.* **2012**, *100* (1), 013504.

(2) Dong, L.; Jia, R.; Xin, B.; Peng, B.; Zhang, Y. Effects of oxygen vacancies on the structural and optical properties of β-Ga_2O_3. *Sci. Rep.* **2017**, *7*, 40160.

(3) Guo, D.; Liu, H.; Li, P.; Wu, Z.; Wang, S.; Cui, C.; Li, C.; Tang, W. Zero-power-consumption solar-blind photodetector based on β-Ga2O3/NSTO heterojunction. *ACS Appl. Mater. Interfaces* **2017**, *9* (2), 1619−1628.

(4) He, H.; Orlando, R.; Blanco, M. A.; Pandey, R.; Amzallag, E.; Baraille, I.; Rérat, M. First-principles study of the structural, electronic, and optical properties of Ga_2O_3 in its monoclinic and hexagonal phases. *Phys. Rev. B: Condens. Matter Mater. Phys.* **2006**, *74* (19), 195123.

(5) Yoshioka, S.; Hayashi, H.; Kuwabara, A.; Oba, F.; Matsunaga, K.; Tanaka, I. Structures and energetics of Ga_2O_3 polymorphs. *J. Phys.: Condens. Matter* **2007**, *19* (34), 346211.

(6) Ghose, S.; Rahman, S.; Hong, L.; Rojas-Ramirez, J. S.; Jin, H.; Park, K.; Klie, R.; Droopad, R. Growth and characterization of β-Ga_2O_3thin films by molecular beam epitaxy for deep-UV photodetectors. *J. Appl. Phys.* **2017**, *122* (9), 095302.

(7) Zheng, X.-Q.; Lee, J.; Rafique, S.; Han, L.; Zorman, C. A.; Zhao, H.; Feng, P. X.-L. Ultrawide Band Gap β-Ga2O3 Nanomechanical Resonators with Spatially Visualized Multimode Motion. *ACS Appl. Mater. Interfaces* **2017**, *9* (49), 43090−43097.

(8) Patil, S. B.; Kim, I. Y.; Gunjakar, J. L.; Oh, S. M.; Eom, T.; Kim, H.; Hwang, S.-J. Phase tuning of nanostructured gallium oxide via hybridization with reduced graphene oxide for superior anode performance in Li-ion battery: an experimental and theoretical study. *ACS Appl. Mater. Interfaces* **2015**, *7* (33), 18679−18688.

(9) Åhman, J.; Svensson, G.; Albertsson, J. A reinvestigation of β-gallium oxide. *Acta Crystallogr., Sect. C: Cryst. Struct. Commun.* **1996**, *52* (6), 1336−1338.

(10) Liu, T.; Feng, Z.; Li, Q.; Yang, J.; Li, C.; Dupuis, M. Role of Oxygen Vacancies on Oxygen Evolution Reaction Activity: β-Ga2O3 as a Case Study. *Chem. Mater.* **2018**, *30* (21), 7714−7726.

(11) Peelaers, H.; Van de Walle, C. G. Brillouin zone and band structure of β-Ga_2O_3. *Phys. Status Solidi B* **2015**, *252* (4), 828−832.

(12) Yang, G.; Jang, S.; Ren, F.; Pearton, S. J.; Kim, J. Influence of high-energy proton irradiation on β-Ga2O3 nanobelt field-effect transistors. *ACS Appl. Mater. Interfaces* **2017**, *9* (46), 40471−40476.

(13) Zhou, W.; Xia, C.; Sai, Q.; Zhang, H. Controlling n-type conductivity of β-Ga_2O_3 by Nb doping. *Appl. Phys. Lett.* **2017**, *111* (24), 242103.

(14) Pearton, S.; Yang, J.; Cary IV, P. H.; Ren, F.; Kim, J.; Tadjer, M. J.; Mastro, M. A. A review of Ga_2O_3 materials, processing, and devices. *Appl. Phys. Rev.* **2018**, *5* (1), 011301.

(15) Oleksak, R. P.; Stickle, W. F.; Herman, G. S. Aqueous-based synthesis of gallium tungsten oxide thin film dielectrics. *J. Mater. Chem. C* **2015**, *3* (13), 3114−3120.

(16) Suzuki, N.; Ohira, S.; Tanaka, M.; Sugawara, T.; Nakajima, K.; Shishido, T. Fabrication and characterization of transparent conductive Sn-doped β-Ga_2O_3 single crystal. *Phys. Status Solidi C* **2007**, *4* (7), 2310−2313.

(17) Fu, L.; Liu, Y.; Hu, P. a.; Xiao, K.; Yu, G.; Zhu, D. Ga2O3 nanoribbons: synthesis, characterization, and electronic properties. *Chem. Mater.* **2003**, *15* (22), 4287−4291.

(18) López, I. a.; Nogales, E.; Méndez, B.; Piqueras, J.; Peche, A.; Ramírez-Castellanos, J.; González-Calbet, J. M. Influence of Sn and Cr doping on morphology and luminescence of thermally grown Ga2O3 nanowires. *J. Phys. Chem. C* **2013**, *117* (6), 3036−3045.

(19) Zhou, S.; Feng, G.; Wu, B.; Jiang, N.; Xu, S.; Qiu, J. Intense infrared luminescence in transparent glass-ceramics containing β-Ga2O3: Ni2+ nanocrystals. *J. Phys. Chem. C* **2007**, *111* (20), 7335−7338.

(20) Jin, S.; Wang, X.; Wang, X.; Ju, M.; Shen, S.; Liang, W.; Zhao, Y.; Feng, Z.; Playford, H. Y.; Walton, R. I.; Li, C. Effect of phase junction structure on the photocatalytic performance in overall water splitting: Ga_2O_3 photocatalyst as an example. *J. Phys. Chem. C* **2015**, *119* (32), 18221−18228.

(21) Ginley, D. S.; Bright, C. Transparent conducting oxides. *MRS Bull.* **2000**, *25* (8), 15−18.

(22) Minami, T. Transparent conducting oxide semiconductors for transparent electrodes. *Semicond. Sci. Technol.* **2005**, *20* (4), S35.

(23) Muhammed, M. M.; Alwadai, N.; Lopatin, S.; Kuramata, A.; Roqan, I. S. High-Efficiency InGaN/GaN Quantum Well-Based Vertical Light-Emitting Diodes Fabricated on β-Ga2O3 Substrate. *ACS Appl. Mater. Interfaces* **2017**, *9* (39), 34057−34063.

(24) Ogita, M.; Higo, K.; Nakanishi, Y.; Hatanaka, Y. Ga_2O_3 thin film for oxygen sensor at high temperature. *Appl. Surf. Sci.* **2001**, *175*, 721−725.

(25) Bartic, M.; Baban, C. I.; Suzuki, H.; Ogita, M.; Isai, M. β-Gallium Oxide as Oxygen Gas Sensors at a High Temperature. *J. Am. Ceram. Soc.* **2007**, *90* (9), 2879−2884.

(26) Li, Y.; Trinchi, A.; Wlodarski, W.; Galatsis, K.; Kalantar-zadeh, K. Investigation of the oxygen gas sensing performance of Ga_2O_3 thin films with different dopants. *Sens. Actuators, B* **2003**, *93* (1−3), 431−434.

(27) Battu, A. K.; Manandhar, S.; Ramana, C. V. Nanomechanical characterization of titanium incorporated gallium oxide nanocrystalline thin films. *Materials Today Nano* **2018**, *2*, 7−14.

(28) Rubio, E. J.; Mates, T. E.; Manandhar, S.; Nandasiri, M.; Shutthanandan, V.; Ramana, C. V. Tungsten Incorporation into Gallium Oxide: Crystal Structure, Surface and Interface Chemistry, Thermal Stability, and Interdiffusion. *J. Phys. Chem. C* **2016**, *120* (47), 26720−26735.

(29) Huda, M. N.; Yan, Y.; Moon, C.-Y.; Wei, S.-H.; Al-Jassim, M. M. Density-functional theory study of the effects of atomic impurity on the band edges of monoclinic WO_3. *Phys. Rev. B: Condens. Matter Mater. Phys.* **2008**, *77* (19), 195102.

(30) Tang, C.; Sun, J.; Lin, N.; Jia, Z.; Mu, W.; Tao, X.; Zhao, X. Electronic structure and optical property of metal-doped Ga_2O_3: a first principles study. *RSC Adv.* **2016**, *6* (82), 78322−78334.

(31) Víllora, E. G.; Shimamura, K.; Yoshikawa, Y.; Ujiie, T.; Aoki, K. Electrical conductivity and carrier concentration control in β-Ga_2O_3 by Si doping. *Appl. Phys. Lett.* **2008**, *92* (20), 202120.

(32) Peelaers, H.; Van de Walle, C. Doping of Ga_2O_3 with transition metals. *Phys. Rev. B: Condens. Matter Mater. Phys.* **2016**, *94* (19), 195203.

(33) Wang, X.; Shen, S.; Jin, S.; Yang, J.; Li, M.; Wang, X.; Han, H.; Li, C. Effects of Zn^{2+} and Pb^{2+} dopants on the activity of Ga_2O_3-based photocatalysts for water splitting. *Phys. Chem. Chem. Phys.* **2013**, *15* (44), 19380−19386.

(34) Zhang, Y.; Yan, J.; Li, Q.; Qu, C.; Zhang, L.; Xie, W. Optical and structural properties of Cu-doped β-Ga2O3 films. *Mater. Sci. Eng., B* **2011**, *176* (11), 846−849.

(35) Zhang, H.; Deng, J.; Duan, P.; Li, R.; Pan, Z.; Bai, Z.; Kong, L.; Wang, J. Effect of Au nanoparticles on the optical and electrical properties of Nb-doped β-Ga_2O_3 film. *Vacuum* **2018**, *155*, 465−469.

DOI: 10.1021/acs.inorgchem.8b03328
Inorg. Chem. 2019, 58, 3707−3716

(36) Dakhel, A. Structural, optical, and opto-dielectric properties of W-doped Ga_2O_3 thin films. *J. Mater. Sci.* **2012**, *47* (7), 3034−3039.
(37) Shannon, R. D. Revised effective ionic radii and systematic studies of interatomic distances in halides and chalcogenides. *Acta Crystallogr., Sect. A: Cryst. Phys., Diffr., Theor. Gen. Crystallogr.* **1976**, *32* (5), 751−767.
(38) Francke, L.; Durand, E.; Demourgues, A.; Vimont, A.; Daturi, M.; Tressaud, A. Synthesis and characterization of Al^{3+}, Cr^{3+}, Fe^{3+} and Ga^{3+} hydroxyfluorides: correlations between structural features, thermal stability and acidic properties. *J. Mater. Chem.* **2003**, *13* (9), 2330−2340.
(39) Chen, D.; Zhang, Y.; Ge, X.; Cheng, Y.; Liu, Y.; Yuan, H.; Guo, J.; Chao, M.; Liang, E. Structural, vibrational and thermal expansion properties of $Sc_2W_4O_{15}$. *Phys. Chem. Chem. Phys.* **2018**, *20* (30), 20160−20166.
(40) Ramana, C. V.; Atuchin, V. V.; Kesler, V.; Kochubey, V.; Pokrovsky, L.; Shutthanandan, V.; Becker, U.; Ewing, R. C. Growth and surface characterization of sputter-deposited molybdenum oxide thin films. *Appl. Surf. Sci.* **2007**, *253* (12), 5368−5374.
(41) Mudavakkat, V.; Atuchin, V.; Kruchinin, V.; Kayani, A.; Ramana, C. Structure, morphology and optical properties of nanocrystalline yttrium oxide (Y2O3) thin films. *Opt. Mater.* **2012**, *34* (5), 893−900.
(42) Kruchinin, V. N.; Perevalov, T.; Atuchin, V. V.; Gritsenko, V.; Komonov, A.; Korolkov, I.; Pokrovsky, L. D.; Shih, C. W.; Chin, A. Optical properties of TiO 2 films deposited by reactive electron beam sputtering. *J. Electron. Mater.* **2017**, *46* (10), 6089−6095.
(43) Singh, D.; Mallesham, B.; Deshinge, A.; Joshi, K.; Ranjith, R.; Balakrishnan, V. Nanomechanical behavior of $Pb(Fe_{0.5-x}Sc_xNb_{0.5})O_3$ multiferroic ceramics. *Mater. Res. Express* **2018**, *5* (11), 116303.
(44) Juma, A. O.; Arbab, E. A.; Muiva, C. M.; Lepodise, L. M.; Mola, G. T. Synthesis and characterization of CuO-NiO-ZnO mixed metal oxide nanocomposite. *J. Alloys Compd.* **2017**, *723*, 866−872.
(45) Rodríguez-Carvajal, J. Recent advances in magnetic structure determination by neutron powder diffraction. *Phys. B* **1993**, *192* (1−2), 55−69.
(46) Atuchin, V. V.; Beisel, N. F.; Galashov, E. N.; Mandrik, E. M.; Molokeev, M. S.; Yelisseyev, A. P.; Yusuf, A. A.; Xia, Z. Pressure-stimulated synthesis and luminescence properties of microcrystalline (Lu, Y) 3Al5O12: Ce3+ garnet phosphors. *ACS Appl. Mater. Interfaces* **2015**, *7* (47), 26235−26243.
(47) Atuchin, V.; Aleksandrovsky, A.; Chimitova, O.; Gavrilova, T.; Krylov, A.; Molokeev, M.; Oreshonkov, A.; Bazarov, B.; Bazarova, J. Synthesis and spectroscopic properties of monoclinic α-Eu2 (MoO4) 3. *J. Phys. Chem. C* **2014**, *118* (28), 15404−15411.
(48) Atuchin, V.; Chimitova, O.; Adichtchev, S.; Bazarov, J.; Gavrilova, T.; Molokeev, M.; Surovtsev, N.; Bazarova, Z. G. Synthesis, structural and vibrational properties of microcrystalline β-RbSm (MoO4) 2. *Mater. Lett.* **2013**, *106*, 26−29.
(49) Kalhori, H.; Porter, S. B.; Esmaeily, A. S.; Coey, M.; Ranjbar, M.; Salamati, H. Morphology and structural studies of WO3 films deposited on SrTiO3 by pulsed laser deposition. *Appl. Surf. Sci.* **2016**, *390*, 43−49.
(50) Stepanov, S.; Nikolaev, V.; Bougrov, V.; Romanov, A. Gallium oxide: Properties and applications - A review. *Rev. Adv. Mater. Sci.* **2016**, *44*, 63−86.
(51) Han, B.; Li, Y.; Guo, C.; Li, N.; Chen, F. Sintering of MgO-based refractories with added WO3. *Ceram. Int.* **2007**, *33* (8), 1563−1567.
(52) Zhang, S. C.; Hilmas, G. E.; Fahrenholtz, W. G. Improved oxidation resistance of zirconium diboride by tungsten carbide additions. *J. Am. Ceram. Soc.* **2008**, *91* (11), 3530−3535.
(53) Oppolzer, H.; Schmelz, H. Investigation of twin lamellae in BaTiO3 ceramics. *J. Am. Ceram. Soc.* **1983**, *66* (6), 444−446.
(54) Wriedt, H. The OW (oxygen-tungsten) system. *Bull. Alloy Phase Diagrams* **1989**, *10* (4), 368−384.
(55) Bale, C.; Bélisle, E.; Chartrand, P.; Decterov, S.; Eriksson, G.; Hack, K.; Jung, I.-H.; Kang, Y.-B.; Melançon, J.; Pelton, A.; Robelin, C.; Petersen, S. FactSage thermochemical software and databases—recent developments. *CALPHAD: Comput. Coupling Phase Diagrams Thermochem.* **2009**, *33* (2), 295−311.
(56) Mengle, K. A.; Shi, G.; Bayerl, D.; Kioupakis, E. First-principles calculations of the near-edge optical properties of β-Ga_2O_3. *Appl. Phys. Lett.* **2016**, *109* (21), 212104.
(57) Rubio, E. J.; Ramana, C. V. Tungsten-incorporation induced red-shift in the bandgap of gallium oxide thin films. *Appl. Phys. Lett.* **2013**, *102* (19), 191913.
(58) Tauc, J.; Grigorovici, R.; Vancu, A. Optical properties and electronic structure of amorphous germanium. *Phys. Status Solidi B* **1966**, *15* (2), 627−637.
(59) Tauc, J. Optical properties and electronic structure of amorphous Ge and Si. *Mater. Res. Bull.* **1968**, *3* (1), 37−46.
(60) Ganesh, I.; Kumar, P. P.; Gupta, A. K.; Sekhar, P. S.; Radha, K.; Padmanabham, G.; Sundararajan, G. Preparation and characterization of Fe-doped TiO_2 powders for solar light response and photocatalytic applications. *Process. Appl. Ceram.* **2012**, *6* (1), 21−36.
(61) Oliveira, H. d. S.; Silva, A. C.; de Mesquita, J. P.; Pereira, F. V.; Lima, D. Q.; Fabris, J. D.; Moura, F. C.; Oliveira, L. C. A novel floating photocatalyst device based on cloth canvas impregnated with iron oxide. *New J. Chem.* **2013**, *37* (8), 2486−2491.
(62) Reshak, A. H.; Alahmed, Z.; Bila, J.; Atuchin, V. V.; Bazarov, B. G.; Chimitova, O. D.; Molokeev, M. S.; Prosvirin, I. P.; Yelisseyev, A. P. Exploration of the electronic structure of monoclinic α-Eu2 (MoO4) 3: DFT-based study and X-ray photoelectron spectroscopy. *J. Phys. Chem. C* **2016**, *120* (19), 10559−10568.
(63) Nandan, B.; Venugopal, B.; Amirthapandian, S.; Panigrahi, B.; Thangadurai, P. Effect of Pd ion doping in the band gap of SnO_2 nanoparticles: structural and optical studies. *J. Nanopart. Res.* **2013**, *15* (10), 1999.
(64) Onuma, T.; Saito, S.; Sasaki, K.; Masui, T.; Yamaguchi, T.; Honda, T.; Higashiwaki, M. Valence band ordering in β-Ga_2O_3 studied by polarized transmittance and reflectance spectroscopy. *Jpn. J. Appl. Phys.* **2015**, *54* (11), 112601.
(65) Santhosh, S.; Mathankumar, M.; Selva Chandrasekaran, S.; Nanda Kumar, A.; Murugan, P.; Subramanian, B. Effect of Ablation Rate on the Microstructure and Electrochromic Properties of Pulsed-Laser-Deposited Molybdenum Oxide Thin Films. *Langmuir* **2017**, *33* (1), 19−33.
(66) Mallesham, B.; Ranjith, R.; Manivelraja, M. Scandium induced structural transformation and B′: B ″cationic ordering in Pb-$(Fe_{0.5}Nb_{0.5})O_3$ multiferroic ceramics. *J. Appl. Phys.* **2014**, *116* (3), 034104.
(67) Li, Y. W.; Sun, J. L.; Meng, X. J.; Chu, J. H.; Zhang, W. F. Structural and optical properties of $Ba(Co_xTi_{1-x})O_3$ thin films fabricatedby sol-gel process. *Appl. Phys. Lett.* **2004**, *85* (11), 1964−1966.
(68) Wu, M.; Wang, Z.; Zhang, T.; Zhang, W. Composition dependence of optical constants in ferroelectric $Ba(Ti_{1-x}, Ni_x)O_3$ thin films by optical transmittance technique. *Thin Solid Films* **2010**, *518* (23), 7007−7011.
(69) Stroud, D.; Ehrenreich, H. Band structure of SiGe: Coherent-potential approximation. *Phys. Rev. B* **1970**, *2* (8), 3197.
(70) Bullett, D. Bulk and surface electron states in WO_3 and tungsten bronzes. *J. Phys. C: Solid State Phys.* **1983**, *16* (11), 2197.

DOI: 10.1021/acs.inorgchem.8b03328
Inorg. Chem. 2019, 58, 3707−3716